

Experimental assessment of velocity and narrow-band measurements in oxy-fuel combustion of pulverized walnut shells[☆]

Burak Özer¹*, Reinhold Kneer, Anna Maßmeyer

RWTH Aachen University, Institute of Heat and Mass Transfer, Augustinerbach 6, Aachen, 52056, Germany

ARTICLE INFO

Keywords:

Oxy-fuel combustion
Self-sustained
Pulverized walnut shell
Swirl flame
LDV
Flame visualization

ABSTRACT

Self-sustained pulverized biomass swirl flames are investigated experimentally under oxy-fuel atmosphere concerning the effect of thermal load, and oxygen content of the oxidizer stream on flame characteristics. Experiments are conducted employing a swirl burner in a down-fired cylindrical chamber. Operating conditions are selected in ranges of thermal loads between 60 kW_{th} to 100 kW_{th} and oxidizer oxygen contents between 25 and 30 vol.-% while keeping the flame stoichiometry constant. Particle velocity profiles are obtained employing non-intrusive 2D laser Doppler velocimetry. Spectrally narrow-band imaging of the near burner region enables the identification of reaction zones via OH* radical emission imaging as well as regions of high particle temperature by imaging their thermal radiation. The results show that the occurrence of an fuel particle recirculation is related to the ratio of the momentum flow rate of swirled secondary stream over the momentum flow rate of the fuel with its carrying stream. By either reinforcing the flame thermal power or lowering the oxidizer oxygen content, the momentum ratio increases, progressively leading to the fuel particle recirculation at the central axis of the flame. In the flames with a recirculation of hot fuel particles towards the burner, homogeneous devolatilization and char combustion regions are observed in the radical emission of OH* and thermal radiation images, respectively.

1. Introduction

Despite the forecast in recent year's world energy outlook (WEO) [1], that the demand for fossil fuels will peak before 2030, the post-peak decline scenarios largely vary, also due to the presumed ongoing coal usage in the energy sector. Thus, besides the effort to decarbonize power generation, a replacement of fossil by biogenic fuels can empower a decline in fossil fuel usage and the related CO₂ emissions. Biomass energy with carbon capture and storage (BECCS), using biomass as the main energy source, even has the potential to decrease the concentration of CO₂ in the atmosphere due to its net negative CO₂ emission [2]. One of the carbon capture and storage (CCS) technologies is oxy-fuel combustion in which combustion takes place in a mixture of CO₂ and O₂. Therefore, the resultant flue gas of oxy-fuel combustion consists primarily of CO₂, water vapour and emissive species such as NO_x and SO_x. Thus, after condensation of the water and removal of the emissive species, CO₂ can be sequestered and stored. More details about oxy-fuel combustion can be found in various reviews, e.g. [3–5].

In the oxy-fuel process, the oxygen content in the oxidizer stream is adjustable, increasing the degree of freedom in tuning the combustion process. For pulverized coal combustion under an oxy-fuel atmosphere,

the effects of different oxygen concentrations in the oxidizer stream have been studied in detail. Becker et al. [6] demonstrated that varying the O₂ concentration between 25 vol.-% and 30 vol.-% influences flame stabilization inside the burner quarl, with the flame base shifting due to changes in recirculation and mixing. Zabrodiec et al. [7] performed flow field measurements using laser Doppler anemometry, and showed that increasing O₂ content from 23 vol.-% to 33 vol.-% enhances axial velocities in the main vortex while reducing velocities in the internal recirculation zone, revealing a clear dependence of the flame's flow field on the oxidizer composition. Burkle et al. [8] used tunable diode laser absorption spectroscopy to measure path-integrated temperatures and species concentrations in a lab-scale combustor. The results show that higher O₂ content leads to lower CO and CH₄ concentrations in the flue gas which indicate improved reaction progress and enhanced burnout due to better mixing of the flows within the combustion chamber. In contrast to the extensive research on coal combustion, experimental studies on pulverized biomass flames remain scarce, especially under oxy-fuel conditions. Moreover, the majority of experimental works on biomass combustion in the literature are limited to the measurements of gas-phase temperature [9,10], and concentration of gas-phase species (e.g. CO₂, CO, O₂) [11,12].

[☆] This article is part of a Special issue entitled: 'MCS13' published in Experimental Thermal and Fluid Science.

* Corresponding author.

E-mail address: burak.oezer@rwth-aachen.de (B. Özer).

A thorough understanding of the underlying mechanisms in biomass swirl flames requires a detailed characterization of a variety of carefully selected operating conditions. In the work of König et al. [13], pulverized biomass flames at thermal powers of 500 kW_{th} and 750 kW_{th} were operated with two different inlet swirl numbers. Their investigations focused on flue gas contents and thermal radiation of the biomass flames at different swirl numbers. However, due to the aerodynamic stabilization of swirl flames, the flow field is crucial parameter that needs to be investigated. Recently, Schneider et al. [14] conducted a comprehensive study on gas-assisted pulverized biomass swirl flames in oxy-fuel atmosphere. Their work demonstrated that the position of both – the combustion zone and the internal recirculation zone at the axis of the flame – shifts towards the burner and becomes more tightly compacted with increasing oxygen content in oxidizer stream.

In the test rig of this study, the first studies with pulverized walnut shell combustion have been conducted to investigate the effects of methane-assistance on the flame start-up procedure employing particle velocity measurements, and narrow-band flame imaging [15]. The measurements show that methane-assistance at the startup of the pulverized walnut shell flame is the deciding parameter for the aerodynamic control of the flame. Even if the methane-assistance is cut a while after the flame is started, the flame can manage to keep its flow field and shape. Previous studies in this chamber and this burner concentrated on the influences of different fuels and, different atmospheres at fixed thermal load of 60 kW_{th} [16–18], also complemented by the numerical studies [19–21]. This study aims to explore the effects of increasing thermal load and oxygen concentrations in the oxidizer stream. A total set of five different flames is presented, with three flames at the same oxidizer composition with an oxygen content of 25 vol. – % and thermal load varying between 60 kW_{th} and 100 kW_{th}, and three flames at constant thermal load of 100 kW_{th} with the oxygen content varying between 25 to 30 vol. – %. Non-intrusive laser-Doppler velocimetry (LDV) is employed to obtain particle velocity profiles at different distances below the burner. Likewise, non-intrusive spectrally narrow-band imaging enables linking the flow field to the devolatilization zones and identifying regions with high particle temperatures.

2. Experimental setup

2.1. Combustion chamber and operating conditions

Experiments are conducted in the pilot-scale down-fired cylindrical combustion chamber (cf. Fig. 1(a) - (b)) in the test facility of the Institute of Heat and Mass Transfer (Lehrstuhl für Wärme und Stoff-übertragung, WSA) at RWTH (Rheinisch-Westfälische Technische Hochschule) Aachen University. The cylindrical design supports a symmetric flow field and strong internal recirculation, allowing particles to remain longer in the chamber and burn out completely. The inner diameter and the length of the chamber are 400 mm and 4200 mm, respectively. Heating elements embedded into the chamber's ceramic wall to sustain a wall temperature of $\approx 1000^\circ\text{C}$ for the experiments. Thus, pilot-scale pulverized solid fuel combustion can be conducted without the need for gas-phase flame assistance. The experiments are performed at the measurement level of the chamber (cf. Fig. 1(c)) with three measurement ports, available for either optical or probe access into the chamber. To protect the optical windows from deposition of fuel and ash particles, a continuous purge flow is introduced and subsequently recaptured through nozzles located at the inner region of each optical access port. The burner is mounted on the vertically traversable burner port whose location can be seen in Fig. 1. a. Thus, at the measurement level, different sections of the flame can be optically accessed by adjusting the vertical position of the burner within the combustion chamber. A flue gas quench section is positioned below the combustion chamber to cool the exhaust gases prior to their discharge

to the stack. Cooling is accomplished via water injection. The opening between the combustion chamber and the flue gas quench is intentionally kept small to prevent the cold quench gases from affecting the flame.

The test facility can be operated in three different modes: air, dry oxy-fuel, and wet oxy-fuel. The air and dry oxy-fuel modes represent once-through operation, using either air or a mixture of CO₂ and O₂ as the oxidizer, respectively. In air mode, compressor air system with a built-in refrigerant dryer provides a clean, dry air to be used in the combustion chamber. In the dry oxy-fuel mode which is employed in this study, oxygen and carbon dioxide are provided from separate supply tanks, and an in-house gas mixer prepares the oxidizer mixture with the desired O₂ content. The wet oxy-fuel mode corresponds to a flue gas recirculation configuration, in which a portion of the flue gas is recycled and enriched with oxygen.

A swirl-type burner with a diffusor (cf. Fig. 2) was employed to build stable self-sustained biomass flames in the combustion chamber. The same burner has been previously employed in investigations of pulverized coal flames under air and oxy-fuel conditions [16,18]. The burner has two concentric annular nozzles (named primary and secondary) through which the oxidizer flow is released into the diffusor region. The primary nozzle concentrically surrounds a central bluff body and delivers the solid fuel particles entrained by the oxidizer stream. The feeding rate of solid fuel particles was controlled by a double-screw feeder, from which the particles were discharged and transported into the primary oxidizer line. To mitigate the risk of spontaneous combustion within the feeder silo, the system is continuously purged with inert gas. During operation, this constant inert gas flow prevents oxidizer backflow from the oxidizer primary stream into the feeder. Consequently, the primary stream is operated with a reduced oxygen concentration. The secondary nozzle is the only nozzle that delivers a swirled oxidizer stream into the chamber. Within the burner body, the secondary stream obtains its swirl in a plenum chamber situated ahead of the nozzle. The swirler assembly includes four axial and four 45°-inclined tangential channels. By redistributing the total flow between these channels, the level of swirl imparted to the secondary stream can be controlled. Detailed illustrations of the burner and its swirler can be found in [6]. The geometric swirl number for all conditions is $S_g = 0.95$ according to the definition (Eq. (1)) by [22]. It represents the ratio between the axial flux of swirl momentum (G_v) and the axial flux of axial momentum (G_u) times the equivalent nozzle radius (r). An $S_g = 0.95$ corresponds to a flow field with an effective swirl angle of about 45°. This swirl number was selected since the previous experiments demonstrated that it yields a stable flame with minimal observable fluctuations. The diameter of the secondary nozzle, $d = 64.0$ mm, is used as the reference length for the description of the axial and radial positions of the measurements taken, i.e. measurements at $H = 0.5d$ are taken 32.0 mm below the dump plane. The tertiary stream is released into the chamber through a gap between the diffusor and burner port. Lastly, the necessary oxygen for the complete combustion is provided by the staging stream, which enters the combustion chamber via the gap between the burner port and the chamber wall. The main purpose of the tertiary and staging streams is to reduce the amount of oxidizing gas injected through the diffusor (by the primary and secondary nozzles), thereby decreasing the axial velocity at the burner. Furthermore, by adjusting the ratio between the oxidizer supplied through the diffusor and that provided by the tertiary stream, the local air ratio can be controlled. This enables the establishment of under-stoichiometric conditions in the near-burner region.

$$S_g = \frac{G_v}{G_u r} \quad (1)$$

The operating conditions of the investigated flames are listed in Table 1. The flames are named based on the thermal load in kW_{th} and the volumetric percentage of oxygen in the oxidizer stream, e.g 100kW-OXY25 flame is 100 kW_{th} flame operating in oxyfuel atmosphere with

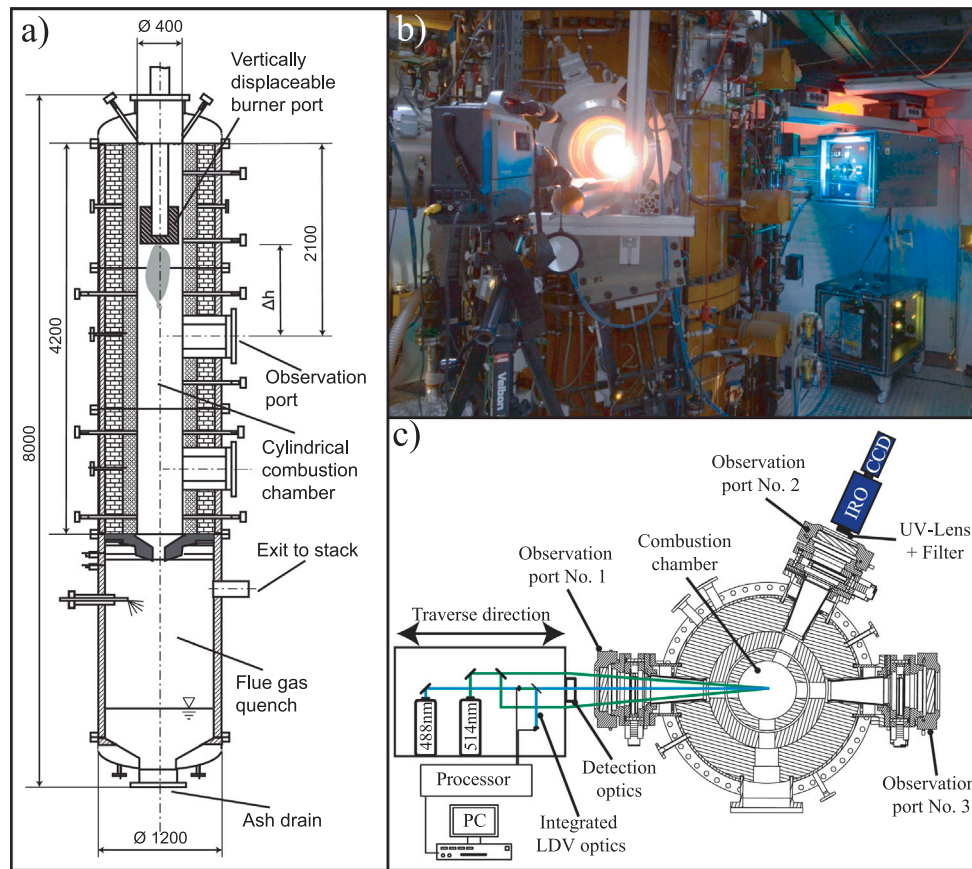


Fig. 1. (a) Cross-sectional illustration of the experimental test facility. (b) Picture of the measurement level at the experimental facility in RWTH. (c) Cross-sectional illustration of the measurement level with LDV and narrow-band imaging setups. All geometrical dimensions are given in millimetres.

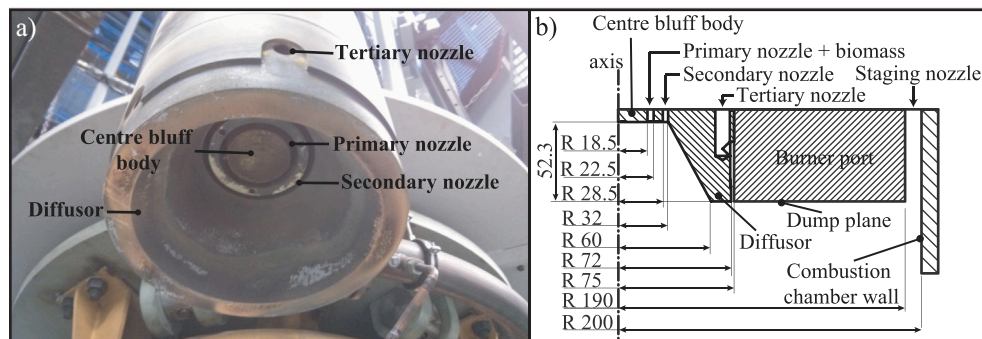


Fig. 2. (a) Picture of the swirl burner. (b) Half cross-sectional view illustrating the traversable burner port and the swirl burner installed at the top of the combustion chamber. The main components — primary (fuel + oxidizer) nozzle, secondary, tertiary, and staging oxidizer inlets, centre bluff body, and diffuser — are labelled. All geometrical dimensions are provided in millimetres.

25 vol.-% oxygen and remaining 75 vol.-% carbon dioxide. Five self-sustained pulverized biomass flames are selected to examine the effect of thermal load (60kW-OXY25, 80kW-OXY25, 100kW-OXY25 flames) and the oxygen content (100kW-OXY25, 100kW-OXY27, 100kW-OXY30 flames) on the flame characteristics. Flame stoichiometry is kept constant for all studied cases by using the same oxygen-fuel ratios (λ) in the oxidizer flow rate calculation. Hence, $\lambda = 1.0$ represents the complete combustion of solid fuel without excess oxygen in the flue gas. Global oxygen-fuel ratio $\lambda_G = 1.3$ accounts for all oxidizer streams provided into the combustion chamber while the local oxygen-fuel ratio $\lambda_L = 0.8$ excludes the staging stream. The volumetric flow rate of the primary stream is set to $8.5 \text{ m}^3 \text{ h}^{-1}$ for all studied flames for stable pulverized fuel feeding. The chemical composition and the microscopic

size distribution of the walnut shells, used as solid fuel in this study, are presented in Table 2. The volume-based cut-off diameters ($d_{V,10}$, $d_{V,50}$, $d_{V,90}$) of the particles, listed in Table 2, are determined by image processing of the microscopic images of fuel samples, as described in Pielsticker et al. [23].

2.2. Measurement techniques

Spectrally narrow-band imaging is used to identify reaction zones for different flame conditions. The experimental setup includes a CCD camera (LaVision) coupled to an image intensifier (IRO, LaVision). To obtain cross-sectional images of the flames, the image intensifier was focused on the centre of the chamber using a UV objective (UV1054B,

Table 1
Operating conditions.

Parameter	Units	60 kW OXY25	80 kW OXY25	100 kW OXY25	100 kW OXY27	100 kW OXY30
biomass mass flow rate	[kg h ⁻¹]	11.4	15.3	19.1	19.1	19.1
flame thermal load	[kW _{th}]	60	80	100	100	100
O ₂ fraction of	[vol. - %]					
primary stream		22.6	22.6	22.6	24.4	27.1
secondary stream		25.0	25.0	25.0	27.0	30.0
tertiary stream		25.0	25.0	25.0	27.0	30.0
staging stream		25.0	25.0	25.0	27.0	30.0
Volumetric flow rate of ^a	[m ³ h ⁻¹]					
primary stream (\dot{Q}_p)		8.5	8.5	8.5	8.5	8.5
secondary stream (\dot{Q}_s)		23.7	34.0	44.3	40.4	35.7
tertiary stream (\dot{Q}_t)		4.2	6.0	7.8	7.1	6.3
staging stream (\dot{Q}_{st})		22.7	30.3	37.9	35.0	31.5
Bulk velocity of ^a	[m s ⁻¹]					
primary stream ($V_{B,p}$)		4.6	4.6	4.6	4.6	4.6
secondary stream ($V_{B,s}$)		9.9	14.2	18.5	16.9	14.9
tertiary stream ($V_{B,t}$)		1.2	1.8	2.3	2.1	1.9
staging stream ($V_{B,st}$)		0.5	0.7	0.9	0.8	0.7
Temperature of	[°C]					
primary/secondary stream		25/40				
tertiary/staging stream		40/900				
Momentum flow rate of	[kg m s ⁻²]					
fuel		57.9	77.8	97.1	97.1	97.1
secondary stream	$\times 10^{-3}$	120.0	247.0	419.4	346.7	268.3
Momentum ratio, I_s/I_f ^b	$\times 10^{-3}$	2.1	3.2	4.3	3.6	2.8

^a STP = Standard temperature (0°C) and pressure (1.013 bar).

^b Ratio of the momentum flow rate of secondary stream over momentum flow rate of solid fuel.

Table 2
Chemical composition, and microscopic size analysis of the employed walnut shells.

Component		a.r. ^c	w.f. ^d	d.a.f. ^e
Carbon	[w.-%]	46.11	50.94	51.32
Hydrogen	[w.-%]	5.58	6.16	6.21
Oxygen ^a	[w.-%]	37.95	41.92	42.36
Nitrogen	[w.-%]	0.10	0.11	0.11
Sulphur	[w.-%]	<0.01	<0.01	<0.01
Water	[w.-%]	9.48	–	–
Ash	[w.-%]	0.66	0.73	–
Volatiles	[%]	72.93	80.57	81.16
HHV ^b	[MJ/kg]	18.445	20.376	20.525
Particle diameter ^f	[µm]	$d_{V,10}$ 101.5	$d_{V,50}$ 140.6	$d_{V,90}$ 178.8

^a Calculated from difference.

^b HHV: higher heating value.

^c a.r.: as received.

^d w.f.: water free.

^e d.a.f.: dry, ash free.

^f volume-based.

Universe Optics) composed of ultraviolet quartz lenses, allowing the flame's ultraviolet radiation to be detected by the CCD camera. The objective has a focal length of 105 mm, resulting in a conversion ratio of 8 pixels per millimetre for the post-processing of the narrow-band images. Two spectrally narrow-band filters, centred at 308 nm and 430 nm (each with a full-width at half-maximum of 10 nm), were mounted in front of the objective. The 308 nm filter was used to capture the spontaneous radiative emission of radical OH (denoted OH*), whereas the 430 nm filter recorded the thermal radiation originating from the black body radiation of fuel, and soot particles. Since OH* is an intermediate species in the hydrocarbon oxidation [24], its emission is associated with the homogeneous combustion of volatiles.

The narrow-band images were recorded as line-of-sight integrated

emissions of electronically excited species. Due to the optically limited access of the combustion chamber, the recorded images exhibit non-zero intensity at the radial boundaries, particularly in the lower regions of interest for analysis, rendering Abel deconvolution unreliable. Therefore, the presented results correspond to line-of-sight integrated radiation, which may overrepresent intensities at axis of the chamber, rather than true cross-sectional distributions such as those obtained by planar laser-induced fluorescence (PLIF).

Narrow-band images cover the same axial and radial region of the combustion chamber for all investigated flames. Image acquisition was carried out using the frame grabber software (DaVis 7.0) provided by the camera manufacturer. Images were recorded at a constant gain and a fixed frame rate of 1.2 Hz, while the gate time of the image intensifier was varied between 250 000 ns to 999 999 ns to account for the different flame intensities. Since the recorded intensity scales linearly with gate time, comparison between measurements with different gate settings was enabled in post-processing by normalizing each image with respect to its applied gate time. For each flame, 340 images were acquired, temporally averaged, and normalized based on the respective gate settings to ensure comparability across all operating conditions.

The particle velocity profiles along the radial axis of the combustion chamber are measured using laser Doppler velocimetry (LDV). A long-range LDV system (ILA R&D GmbH) designed specifically for this combustion chamber is operated in backscattered mode. Two laser heads (Coherent Genesis CX-SLM series) at wavelengths of 488 nm and 514 nm are operated to simultaneously determine axial and tangential particle velocities, respectively. Each of the two laser head outputs is divided by Bragg cells into two beams, resulting in a total of four beams, with a frequency shift of 40 MHz applied to one beam from each pair. All four laser beams were individually focused and directed to form the measurement volume via a combination of optical components (right angle prisms, singlet lenses) without optical fibre cables which maximize power efficiency. Thus, each beam contributes with a power of ≈ 700 mW to the ellipsoidal measurement volume, which is positioned approximately 1600 mm from the front panel of the LDV

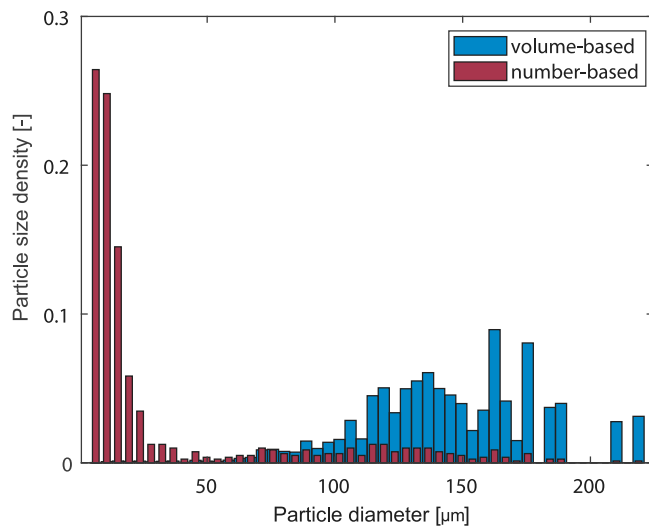


Fig. 3. Particle size distribution of walnut shell particles in volume-based and number-based representations.

system to enable measurements inside the combustion chamber. The ellipsoidal measurement volumes of 488 nm and 514 nm laser couples have a width of 135 μm to 150 μm and a length of 1600 μm to 1800 μm , respectively.

For the collection of Doppler signals, the scattered light at the ellipsoidal measurement volume is captured by optical components (lenses and dichroic beamsplitter) and routed via fibre optics to photomultiplier tubes (PMTs). Bandpass filters are placed between fibre cable ends and the PMTs to suppress undesired wavelength components of the light and to improve the signal-to-noise ratio of the Doppler signal. PMTs are used to amplify very weak light signals and convert them to electrical signals. The voltage on the PMTs are adjusted between 600 V to 1200 V depending on the particle size and concentration on the intersection of optical paths of the laser beams and receiving optics. These output signals of PMTs are then digitized and processed through a Dantec BSA P80 signal processor based on the user input in the BSA flow software.

The LDV system can be traversed in the radial direction. Thus, the particle velocity measurements are performed across the radial axis at the five distances below the burner ($H = 0.3 d, 0.5 d, 1.0 d, 2.0 d, 4.0 d$). The radial resolution of the measurements is adjusted between 1 mm to 20 mm based on the spatial gradients in the velocity profiles. At each radial measurement point, burst signals are collected for 60 s and subsequently processed by the Dantec BSA flow software to obtain the velocity data. The average data rate obtained at each measurement point varies with the local particle number density in the combustion chamber, and the corresponding profiles are presented in Figure A.1 in the Appendix.

Solid fuel particles are used as flow tracers for LDV measurements. Fig. 3 compares the number-based and volume-based particle size distributions of the fuel. As clearly shown, the number-based mean particle diameter $d_{N,50}$ is below 15 μm , indicating that the majority of the fuel particles act as effective flow tracers ($St < 1$). However, in backscattered LDV measurements, larger particles scatter Doppler bursts with significantly higher intensities than smaller ones. To protect PMTs from saturation, sensitivity (high voltage to the PMTs) is set according to the highest scattered intensities. This adjustment leads LDV to favour the burst signals of large particles over those of small particles. Thus, it should be noted that the mean velocities reported in this study represent particle motion, and may not fully capture details of the gas flow field.

3. Results and discussion

In the sections below, the impact of increasing flame thermal power and oxidizer oxygen content on the fuel particle's trajectories, and flame structure is discussed. Radial profiles of dimensionless axial and tangential particle velocities are shown in Fig. 4 for the three OXY25 flames at 60, 80 and 100 kW_{th} as well as one OXY30 flame at 100 kW_{th} . The measured mean velocities are converted to non-dimensional form using the reference velocities which are the mean of the bulk velocities of primary and secondary streams for axial velocity profiles ($\bar{U}_{\text{ref}} = (U_{B,p} + U_{B,s})/2$), and the bulk velocity of secondary stream for tangential velocity profiles ($\bar{V}_{\text{ref}} = V_{B,s}/2$). Bulk velocities of each stream (cf. Table 1) are calculated as: $V_{B,i} = \dot{Q}_i/A_i$, where \dot{Q}_i is the volumetric flow rate of stream i and A is the cross sectional area where the stream i is released into the combustion chamber. The LDV measurements are conducted at five different axial distances below the burner port: $H = 0.3, 0.5, 1.0, 2.0$, and $4.0 d$ – except the 80 kW_{th} flame, where the velocity profile at $H = 4.0 d$ is excluded due to its poor data rate in the measurements. The spectrally narrow-band images of five flames are separated and displayed in two groups: 60, 80 and 100 kW_{th} flames under same oxy-fuel atmospheres in Fig. 5, and 100 kW_{th} flames with three different oxy-fuel atmospheres in Fig. 6. Both images – OH* radical emission and thermal radiation – are taken through the same port and capture the same half section of the axisymmetric flame. For a better visual representation, the OH* images are mirrored. Moreover, to correlate particle velocity profiles and reaction zones, the OH* images include markers indicating the radial positions and magnitudes of the peak axial and tangential velocities (taken from Fig. 4). Thus, the radial trajectory of the main vortex, represented by the positions of peak axial velocities, can be evaluated with respect to the reactive zone of the flame. Radial axis of Figures (r/d) are also in non-dimensional form similar to the axial distances below the burner port (H/d).

3.1. Discussion of increasing thermal power

In the dimensionless velocity profiles of the OXY25 flames (cf. Fig. 4(a)–(c)), two different flame patterns can be observed, which are directly related to the (non-)existence of recirculation of solid fuel particles towards the burner, herein denoted as particle recirculation zone (PRZ). Regarding the profiles around the centre ($r/d = 0$), negative velocities are only observed for the 80 kW_{th} flame at $H = 2.0 d$ and the 100 kW_{th} flame below $H = 1.0 d$. Thus, it is observed that the higher the thermal load, the closer the PRZ reaches towards the burner. In the shear zones around the PRZ, i.e. where the particles' axial trajectory changes direction, the tangential velocities increase, and contract towards the chamber axis. For 80 kW_{th} flame, PRZ develops between $H = 1.0$ – $2.0 d$ where the highest tangential velocity shifts from $r/d = 1.1$ to $r/d = 0.8$ with an increase in magnitude from $\bar{V}/\bar{V}_{\text{ref}} = 0.46$ to 0.54. This increase in velocity is only observed for the flames with PRZ and attributed to the conservation of angular momentum in the rotating motion of the fluid flow. With no PRZ in 60 kW_{th} flame, the peak velocities of the axial and tangential velocity profiles, i.e. the main vortex of the flame, continuously spread outwards towards the chamber wall, where the main vortex merges with the staging stream.

The narrow-band images (cf. Fig. 5) yield a similar picture. With increasing thermal load from 60 kW_{th} to 100 kW_{th} , the OXY25 flames show an increase of intensity for OH* radical emission (left half of narrow-band images in Fig. 5) from as well as thermal radiation (right half of narrow-band images in Fig. 5) at the central axis $r/d = 0$. The recirculation of hot particles towards the burner yields higher flame intensities (OH* radical emission as well as thermal radiation) in the PRZ for both 100 kW_{th} and 80 kW_{th} flames. Since the 60 kW_{th} flame lacks a PRZ, its reactive zone is restricted to its main vortex only. Furthermore, the recirculation provides heat to the near burner region, leading to an earlier volatile release. At 100 kW_{th} , both OH* radical emission and thermal radiation already start in the quail which can

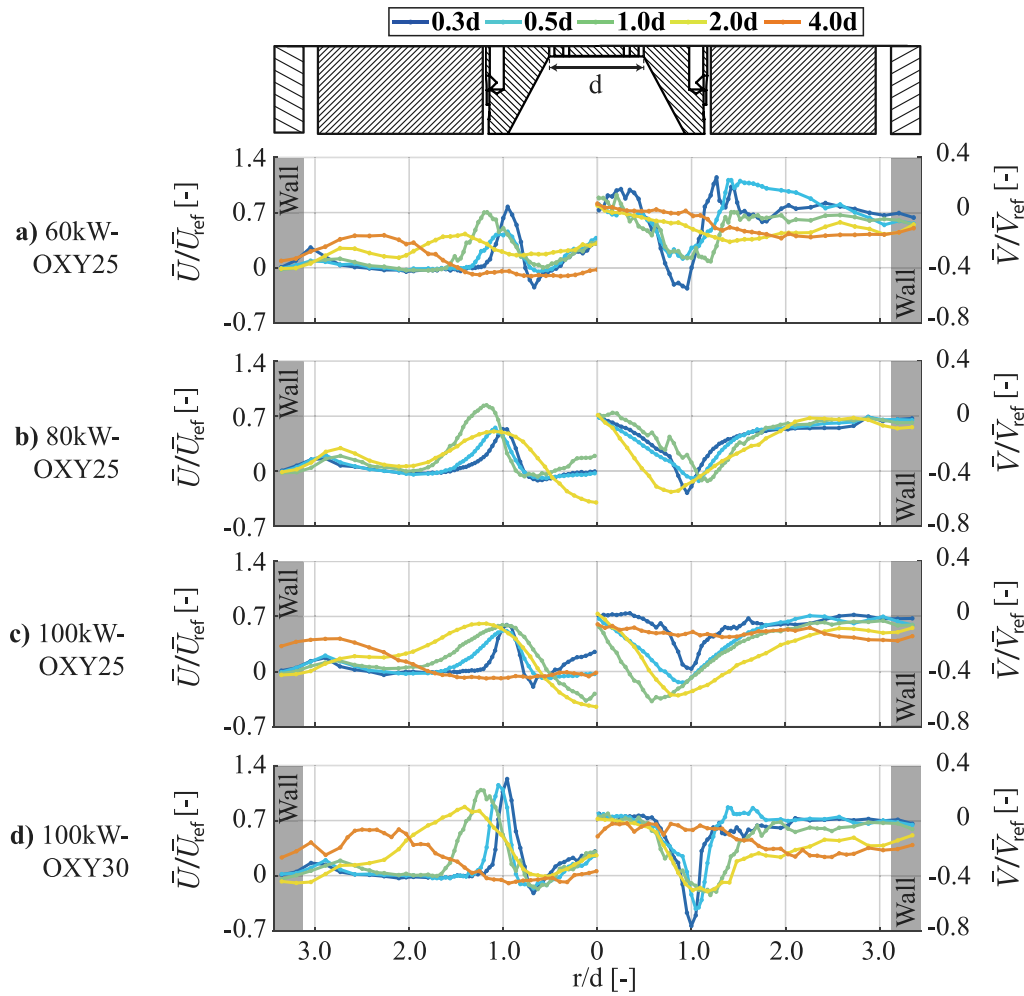


Fig. 4. Dimensionless mean velocity profiles obtained from the LDV measurements of the axial \bar{U} and tangential \bar{V} velocity components for the flames: (a) 60kW-OXY25, (b) 80kW-OXY25, (c) 100kW-OXY25, (d) 100kW-OXY30. Positive values of axial velocity profiles represent a downward velocity in the combustion chamber. Grey shaded regions at $r > 3.125d = 200\text{ mm}$ represents measurements inside the observation port.

be seen below the edge of the diffuser at $r/d = 0.75$. This suggests that the flame stabilizes near the diffuser, enabling early ignition of the biomass particles. With regard to the above observations, it can be concluded that for the investigated flames, an increasing thermal load leads to the formation of a PRZ, that intensifies with a further increase. In parallel, the release of volatiles shifts in the direction of the burner, as the recirculating combustion products reach the area close to the burner and lead to a higher particle heating rate there.

The velocity markers in Fig. 5 show the radial trajectory of the main vortex between $H = 0.3 - 2.0d$. For all the flames, the trajectory of the main vortices follows the progression of OH^* radical emission of the corresponding flames. The main vortex of the 60kW_{th} flame shifts away from the centre axis of the chamber while the main vortex of flames with PRZ stay close to the centre axis. By observing the change in marker size, strong increases in axial velocity can be identified between $H = 0.5d$ and $H = 1.0d$ for both the 60kW_{th} and 80kW_{th} flames, as shown in Fig. 4. It is attributed to the thermal gas-phase expansion, associated with the high combustion temperatures of volatile matters, which manifest in OH^* radical emission observed between $H = 0.5 - 1.0d$ in Fig. 5. Due to the early volatile release of the 100kW_{th} flame inside the diffuser, no sharp increase is observed below the diffuser, neither for OH^* radical emission, nor for the axial velocity.

3.2. Discussion of increasing oxygen content

To explore the effect of oxygen content in the oxidizer streams,

velocity measurements of the flames with the same thermal load of 100kW_{th} are compared for different oxygen contents (OXY25 and OXY30) in Fig. 4(c) - (d). While a PRZ is observed between 1.0–4.0d for the OXY25 flame, the OXY30 flame has no PRZ, similar to the 60kW-OXY25 flame. At the axis of the OXY30 flame ($r/d = 0$) the mean axial velocities have non-zero values throughout the chamber until $H = 4.0d$ where the stagnation point ($\bar{U}/\bar{U}_{\text{ref}} = 0$) is observed. Both velocity components – axial and tangential – show that the main vortex of the OXY30 flame shifts away from the centre with a decrease in the peak value.

As an intermediate step between the OXY25 and the OXY30 flames, the narrow-band images for the OXY27 flame are provided for discussion. It is observed that with an increase in oxygen content, the reaction zones move towards the burner, both at the axis ($r/d = 0$) and below the edge of the diffuser ($r/d = 0.75$). In the OXY25 flame, the highest intensities are observed between $H = 1.0 - 2.0d$ whereas the positions of the highest intensities move gradually closer to the burner in OXY27 and OXY30 flames. This is attributed to the early ignition of fuel particles due to the higher oxygen availability in the flame. Moreover, the decrease in the volumetric oxidizer flow rate at the inlet (cf. Table 1) drops the thermal inertia of the inlet gas flow and so it leads to higher local flame temperature and thermal radiation close to the burner. Although all three 100kW_{th} flames have the same fuel mass flow rate the corresponding flame radiation emission (in arbitrary units) ranges from 5000 (OXY25) over 10000 (OXY27) to 30000 (OXY30).

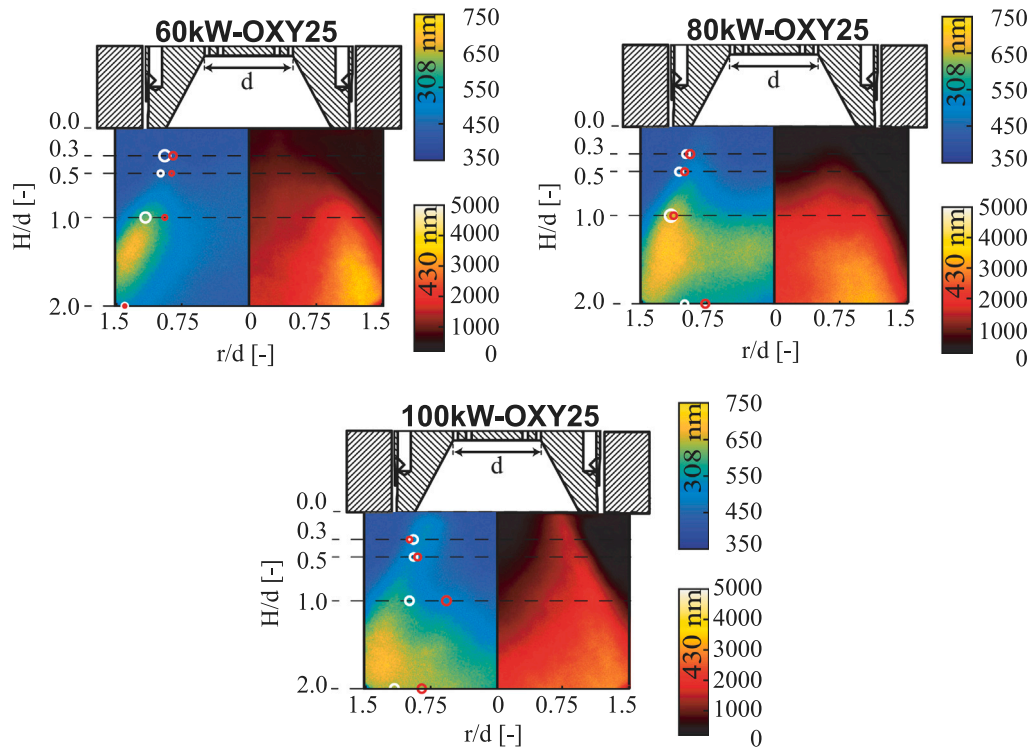


Fig. 5. Temporally averaged spectrally narrow-band emission images of three walnut shell flames with three different thermal loads under same oxy-fuel atmospheres: 60kW-OXY25, 80kW-OXY25 100kW-OXY25. Parula and hot colour-schemes are selected for 308 nm (OH^* luminosity [a.u.]) and 430 nm (Thermal radiation [a.u.]) images, respectively. Hollow markers, velocity markers, represent the radial positions of the highest measured particle velocities (white: axial velocity, red: tangential velocity) at the corresponding axial distances below the burner port (c.f Fig. 4). The sizes of the hollow marks are set proportional to the value of the highest dimensionless measured particle velocities.

The OXY30 flame exhibits the highest intensities of the OH^* radical emission just at the outlet of the diffuser at $r/d = 0.75$, indicating that a strong biomass devolatilization, as well as strong gas-phase expansion, already starts inside the diffuser. This strong gas-phase expansion also explains the difference between the axial velocities of OXY25 and OXY30 flames. Although the OXY30 flame has lower oxidizer flow rates than the OXY25 flame, the axial velocity at $H = 0.3d$ in OXY30 is almost twice as high as that in OXY25. Moreover, a clear shift of the intense radiation zones in OH^* radical emission – away from the axis – is observed, in agreement with the changes in the velocity profiles seen in the velocity markers' radial position change.

Overall, the velocity measurements show that both thermal load and oxygen content significantly influence the development of PRZ and, consequently, the flame stabilization at the diffuser. This can be explained by the variations in the momentum ratio between the flame conditions in Table 1. As the ratio increases from $I_s/I_f = 2.1 \times 10^{-3}$ to $I_s/I_f = 4.3 \times 10^{-3}$ with thermal power increasing from 60kW_{th} to 100kW_{th}, the intensifying formation of a recirculation zone can be observed for the OXY25 flames. This behaviour aligns also well for the cases where the momentum ratio decreases from $I_s/I_f = 4.3 \times 10^{-3}$ for 100kW-OXY25 flame to $I_s/I_f = 2.8 \times 10^{-3}$ 100kW-OXY30 flame. The recirculation zone vanishes when the oxygen contents in the oxidizer stream are increased from 25 to 30 vol.-% for the 100kW_{th} flames. However, aerodynamics at the burner nozzle is not the only parameter responsible for the flame shape. The momentum ratio is larger for 100kW-OXY30 than for 80kW-OXY25. The latter exhibits a recirculation zone, while the former does not. This indicates, that other parameters, such as the availability of oxygen in the vicinity of the burner also play a crucial role in shaping the flame, i.e. the increase in oxygen content leads to far higher flame intensities close to the burner (cf. Fig. 6 for 430 nm).

4. Conclusions

In the present study, the effects of flame thermal power and oxidizer oxygen content on the fuel particle's trajectories, and flame structure of pulverized walnut shell flames are investigated. Spectrally narrow-band imaging and laser Doppler velocimetry measurements are conducted for five different operating conditions with identical stoichiometric conditions.

The experimental results of OXY25 flames show that the thermal power of the flame has a significant effect on the flame characteristics, mainly depending on the ratio of momentum flow rates of the swirled secondary and solid fuel transporting streams. Among three OXY25 flames, a PRZ is developed only in 80kW_{th} and 100kW_{th} flames. Observed PRZs are not stabilized at the bluff body of the burner, and extend between $H = 1.0d$ and $H = 4.0d$. The existence of a PRZ has a homogenizing effect on the flame concerning volatile release and thermal radiation. On the other hand, varying the oxygen content in the oxidizer stream affects significantly all three investigated flame's, showing up in: Particle velocities, OH^* radical emission, and thermal radiation. Although the PRZ vanishes as the oxygen content increases from 25 to 30 vol.-%, the reactive zone of the flames shift into the diffuser, so the flame stabilization at the diffuser improves. Thus, the degree of freedom oxy-fuel combustion provides on the oxygen content in the oxidizer stream is proven to be advantageous since the pulverized biomass flame has a high sensitivity to the oxygen content.

Besides these insights on the combustion behaviour under the investigated operating conditions, the quantitative radial profiles of particle velocity provide a unique dataset for the validation of numerical studies on biomass combustion, paving the way for a transition towards net-zero or negative emissions in the solid-fuel based energy sector.

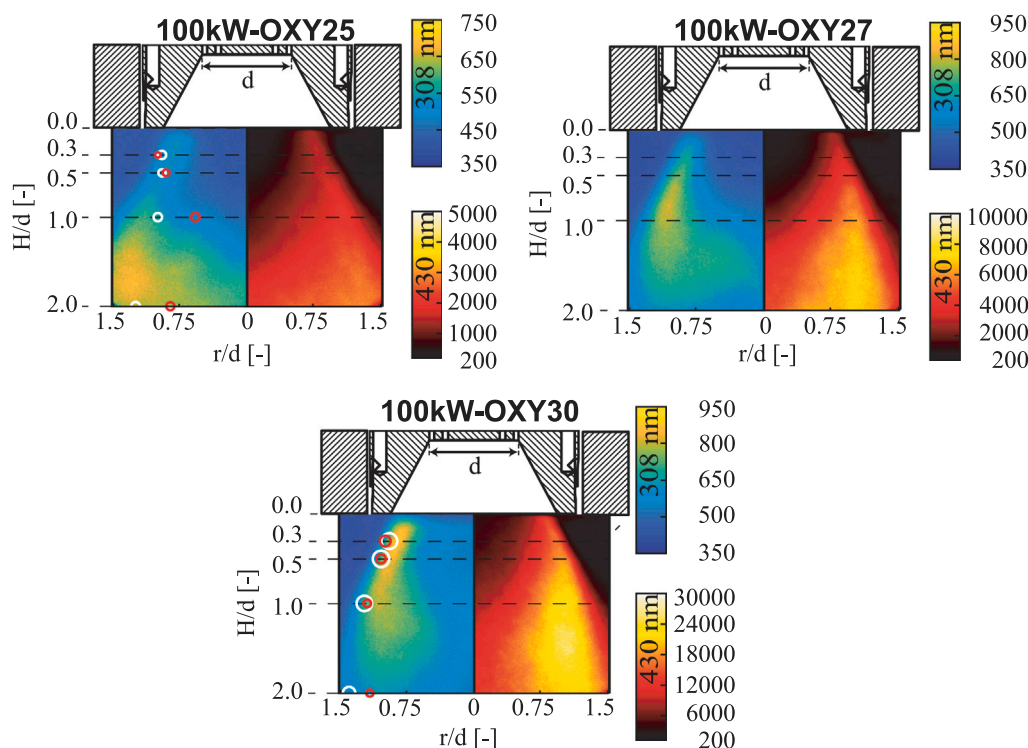


Fig. 6. Temporally averaged spectrally narrowband emission images of three 100 kW walnut shell flames under different oxy-fuel atmospheres: 100kW-OXY25, 100kW-OXY27 100kW-OXY30. Parula and hot colour-schemes are selected for 308 nm (OH^* luminosity [a.u.]) and 430 nm (Thermal radiation [a.u.]) images, respectively. Hollow markers, velocity markers, represent the radial positions of the highest measured particle velocities (white: axial velocity, red: tangential velocity) at the corresponding axial distances below the burner port (c.f Fig. 4). The sizes of the hollow marks are set proportional to the value of the highest dimensionless measured particle velocities. Velocity markers are omitted for the 100kW-OXY27 flame due to the lack of LDV measurements.

CRediT authorship contribution statement

Burak Özer: Writing – review & editing, Writing – original draft, Methodology, Investigation. **Reinhold Kneer:** Writing – review & editing, Supervision, Project administration. **Anna Maßmeyer:** Writing – review & editing, Supervision, Project administration, Methodology.

Declaration of competing interest

The authors declare that they have no known competing financial interests or personal relationships that could have appeared to influence the work reported in this paper.

Acknowledgements

This work has been funded by the German Research Foundation (DFG) - Project number 215035359 - TRR 129 “Oxyflame”. The authors also acknowledge the valuable support of M. Ecker, B. Thalheim, T. Grooten, P. Conzeth, T. Baltaci, R. Solana Gomez, M. Koch, H. Askarizadeh Ravizi and S. Pielsticker during the experimental data gathering process.

Appendix A. Supplementary data

Supplementary material related to this article can be found online at <https://doi.org/10.1016/j.expthermflusci.2025.111658>.

Data availability

Data will be shared in RWTH Aachen university library website.

References

- [1] IEA, *World Energy Outlook 2024*, IEA, 2024, p. 398.
- [2] C. Gough, P. Thornley, S. Mander, N. Vaughan, T. Falano (Eds.), *Biomass Energy and Carbon Capture and Storage (BECCS): Unlocking Negative Emissions*, First ed., John Wiley & Sons, Hoboken NJ, 2018.
- [3] G. Scheffknecht, L. Al-Makhadmeh, U. Schnell, J. Maier, Oxy-fuel coal combustion—A review of the current state-of-the-art, *Int. J. Greenh. Gas Control.* 5 (2011) S16–S35, <http://dx.doi.org/10.1016/j.ijggc.2011.05.020>.
- [4] M.A. Nemitallah, M.A. Habib, H.M. Badr, S.A. Said, A. Jamal, R. Ben-Mansour, E.M.A. Mokheimer, K. Mezghani, Oxy-fuel combustion technology: current status, applications, and trends, *Int. J. Energy Res.* 41 (12) (2017) 1670–1708, <http://dx.doi.org/10.1002/er.3722>.
- [5] L. Chen, S.Z. Yong, A.F. Ghoniem, Oxy-fuel combustion of pulverized coal: Characterization, fundamentals, stabilization and CFD modeling, *Prog. Energy Combust. Sci.* 38 (2) (2012) 156–214.
- [6] L.G. Becker, H. Kosaka, B. Böhm, S. Doost, R. Knappstein, M. Habermehl, R. Kneer, J. Janicka, A. Dreizler, Experimental investigation of flame stabilization inside the swirl of an oxyfuel swirl burner, *Fuel* 201 (2017) 124–135, <http://dx.doi.org/10.1016/j.fuel.2017.02.051>.
- [7] D. Zabrodiec, J. Hees, G. Möller, O. Hatzfeld, R. Kneer, Pulverized coal swirl flames in oxy-fuel conditions: Effects of oxidizer O_2 concentration on flow field and local gas composition, *Proc. Combust. Inst.* 37 (4) (2019) 4471–4478.
- [8] S. Bürkle, L. Becker, A. Dreizler, S. Wagner, Experimental investigation of the flue gas thermochemical composition of an oxy-fuel swirl burner, *Fuel* 231 (2018) 61–72, <http://dx.doi.org/10.1016/j.fuel.2018.05.039>.
- [9] C.T. Salinas, Y. Pu, C. Lou, D.B. dos Santos, Experiments for combustion temperature measurements in a sugarcane bagasse large-scale boiler furnace, *Appl. Therm. Eng.* 175 (2020) 115433, <http://dx.doi.org/10.1016/j.applthermaleng.2020.115433>.
- [10] R. Weber, Y. Poyraz, A.M. Beckmann, S. Brinker, Combustion of biomass in jet flames, *Proc. Combust. Inst.* 35 (3) (2015) 2749–2758, <http://dx.doi.org/10.1016/j.proci.2014.06.033>.
- [11] M. Choi, X. Li, K. Kim, Y. Sung, G. Choi, Detailed in-furnace measurements in a pulverized coal-fired furnace with combined woody biomass co-firing and air staging, *J. Mech. Sci. Technol.* 32 (9) (2018) 4517–4527, <http://dx.doi.org/10.1007/s12206-018-0848-7>.

- [12] J. Ballester, J. Barroso, L.M. Cerecedo, R. Ichaso, Comparative study of semi-industrial-scale flames of pulverized coals and biomass, *Combust. Flame* (2005) <http://dx.doi.org/10.1016/j.combustflame.2005.02.010>.
- [13] D. König, M. Richter, J. Ströhle, B. Eppe, Stability and flame structure analysis of a semi-industrial swirl-stabilized oxy-fuel combustion chamber system for biomass, *Energies* 18 (6) (2025) <http://dx.doi.org/10.3390/en18061513>.
- [14] H. Schneider, M. Bonarens, J. Hebel, H. Hamel, J. Emmert, B. Böhm, S. Wagner, R. Kneer, A. Dreizler, Combined flow, temperature and soot investigation in oxy-fuel biomass combustion under varying oxygen concentrations using laser-optical diagnostics, *Fuel* 362 (2024) 130771, <http://dx.doi.org/10.1016/j.fuel.2023.130771>.
- [15] B. Özer, D. Zabrodiec, R. Kneer, A. Maßmeyer, Experimental investigation of 40 kwth methane-assisted and self-sustained pulverized biomass flames, *Proc. Combust. Inst.* 39 (3) (2023) 3343–3351, <http://dx.doi.org/10.1016/j.proci.2022.07.112>.
- [16] J. Hees, D. Zabrodiec, A. Maßmeyer, M. Habermehl, R. Kneer, Experimental investigation and comparison of pulverized coal combustion in CO₂/O₂- and N₂/O₂-atmospheres, *Flow, Turbul. Combust.* 96 (2) (2016) 417–431.
- [17] A. Maßmeyer, D.M. Zabrodiec, J. Hees, T. Kreitzberg, O. Hatzfeld, R. Kneer, Flame pattern analysis for 60kWth flames under conventional air-fired and oxy-fuel conditions for two different types of coal, *Fuel* 271 (2020) 117457.
- [18] D. Zabrodiec, L.G. Becker, J. Hees, A. Maßmeyer, M. Habermehl, O. Hatzfeld, A. Dreizler, R. Kneer, Detailed analysis of the velocity fields from 60 kW swirl-stabilized coal flames in CO₂/O₂- and N₂/O₂-atmospheres by means of laser Doppler velocimetry and particle image velocimetry, *Combust. Sci. Technol.* 189 (10) (2017) 1751–1775.
- [19] H. Nicolai, X. Wen, F. Miranda, D. Zabrodiec, A. Maßmeyer, F. di Mare, A. Dreizler, C. Hasse, R. Kneer, J. Janicka, Numerical investigation of swirl-stabilized pulverized coal flames in air and oxy-fuel atmospheres by means of large eddy simulation coupled with tabulated chemistry, *Fuel* (2020) 119429, <http://dx.doi.org/10.1016/j.fuel.2020.119429>.
- [20] A. Sadiki, S. Agrebi, M. Chrigui, S. Doost, R. Knapstein, F. di Mare, J. Janicka, A. Maßmeyer, D. Zabrodiec, J. Hees, R. Kneer, Analyzing the effects of turbulence and multiphase treatments on oxy-coal combustion process predictions using LES and RANS, *Chem. Eng. Sci.* 166 (2017) 283–302, <http://dx.doi.org/10.1016/j.ces.2017.03.015>.
- [21] H. Askarizadeh, S. Pielsticker, H. Nicolai, B. Özer, R. Kneer, C. Hasse, A. Maßmeyer, Influence of the devolatilisation kinetics on the numerical simulation of pulverised fuel swirl flames under oxyfuel conditions, *Fuel* 393 (2025) 135177, <http://dx.doi.org/10.1016/j.fuel.2025.135177>.
- [22] N.A. Chigier, J.M. Beer, Velocity and static-pressure distributions in swirling air jets issuing from annular and divergent nozzles, *J. Basic Eng.* 86 (4) (1964) 788–796, <http://dx.doi.org/10.1115/1.3655954>.
- [23] S. Pielsticker, G.H. Möller, B. Gövert, T. Kreitzberg, O. Hatzfeld, Ö. Yönder, V. Angenent, C. Hättig, R. Schmid, R. Kneer, Influence of biomass torrefaction parameters on fast pyrolysis products under flame-equivalent conditions, *Biomass Bioenergy* 119 (2018) 392–410, <http://dx.doi.org/10.1016/j.biombioe.2018.08.014>.
- [24] M. Xia, D.M. Zabrodiec, P. Scoufflaire, B. Fiorina, N. Darabiha, Experimental and numerical studies of pulverized coal devolatilization and oxidation in strained methane/air flames, *Proc. Combust. Inst.* 36 (2) (2017) 2123–2130.